Study of a Multi-Active Bridge Converter for a Domestic Electrical Grid

Abdennour Merrouche, Thierry Talbert, Daniel Matt, Thierry Martiré, Guillaume Pellecuer

pcim
EUROPE

Study of a Multi-Active Bridge Converter for a Domestic Electrical Grid.

Abdennour Merrouche[1,2], Thierry Talbert[1], Daniel Matt[2], Thierry Martiré[2], Guillaume Pellecuer[2]

[1] PROMES-CNRS, UPR 8521, Perpignan University Via Domitia, France
[2] IES, UMR 5214, Montpellier University, France

Corresponding author: Abdennour Merrouche, abdennour.merrouche@promes.cnrs.fr
Speaker: Abdennour Merrouche, abdennour.merrouche@promes.cnrs.fr

Abstract

This article presents the design and development of a three-port, three-phase Multi-Active Bridge (MAB) converter adapted for domestic applications. The primary goal is to establish an autonomous electrical energy storage system utilizing photovoltaic (PV) sources and hydrogen as the storage medium. The converter is strategically designed to facilitate energy exchanges between different renewable energy sources and the electrical loads within the structure. Composed of three three-phase inverters and a transformer for magnetic coupling, each port enables bidirectional power flow and is galvanically isolated. Energy flow regulation is achieved through phase shifting of control commands among the three inverters. This type of converter enables enhanced flexibility and efficiency in integrating renewable energy sources with domestic energy systems, thereby advancing the transition towards sustainable energy applications.

1 Introduction

With the acceleration of climate change, the importance of prioritizing the use of renewable energy sources to reduce CO2 emissions from fossil fuels has become imperative [1]. However, despite the considerable advantages of renewable energies, their intermittent nature, dependent on weather conditions, poses a major limitation. To overcome this intermittency, the use of energy storage means appears as a promising solution.

Currently, batteries are the most commonly used energy storage devices, particularly in the context of photovoltaic installations. However, it is essential to explore other energy storage alternatives in order to optimally and sustainably meet the increasing demand for renewable energy.

Hydrogen is emerging as a promising solution for energy storage, due to its remarkable physical properties as well as its non-toxic and non-polluting nature [2]. Furthermore, its abundant availability on Earth makes it an attractive candidate. The storage system would involve the use of an electrolyzer to produce hydrogen through electrolysis, as well as a fuel cell to regenerate electrical energy from the stored hydrogen.

In [3], a simulation of annual photovoltaic production and average annual consumption for four people shows that during the winter period, photovoltaic production is not sufficient to cover domestic consumption, while there is a surplus of production during the summer. The idea would therefore be to convert this surplus produced in summer into hydrogen, in order to generate electrical energy during the winter period. Hydrogen thus presents a viable solution for long-term storage.

Furthermore, the use of these different energy sources requires a power conversion system capable of interfacing these sources. To enable this interconnection, a multi-source converter is necessary. The two most commonly used structures are Fig. 1 : the first is the grid architecture using a DC voltage bus [4], where different conversion stages are applied for each source and the converters are connected to the common voltage bus. The second structure is the multiport structure. Among the multiport topologies, the Multi-Active Bridge (MAB) stands out as an extension of the dual-active bridge (DAB) [5]. The MAB consists of H-bridges

magnetically coupled by a transformer. The advantages of this topology include high power density, bidirectional power transfer, and galvanic isolation between the sources.

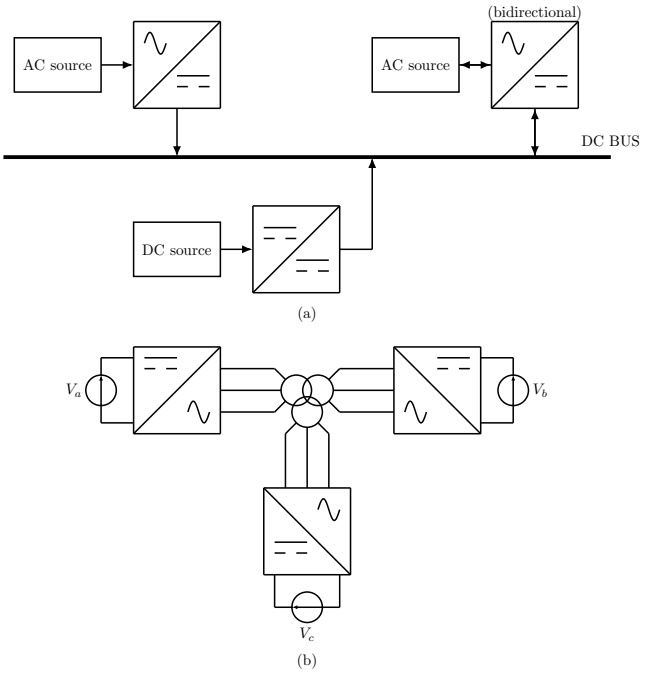

Fig. 1: (a) DC bus grid architecture, (b) Multiport structure.

In this study, the converter choice focused on a specific multiport converter: a three-port three-phase multi-active bridge.

2 Multi-Active Bridge : Theoretical Study

2.1 Structure of the converter

A demonstration of concept viability has been accomplished through the integration of three energy sources utilizing a specialized converter designed for this specific application. In Fig. 2, the schematic illustrates the interconnection of the energy sources via three-phase inverters (A, B and C) and a custom-designed transformer acting as a coupling element.

Each inverter generates a magnetic flux within the transformer. In a balanced state, the magnetic fluxes generated by the three inverters nullify each other, resulting in minimal power exchange. However, by fine-tuning the control parameters of the inverters to manipulate the phase difference between their control commands, we induce a magnetic imbalance, enabling the transfer of energy from one source to another. This principle, known as ”phase-shift” control, forms the basis of our approach.

The transformer plays a crucial role in the converter setup. Its successful implementation demands meticulous modeling and precise dimensioning.

2.2 Power Flow Expression

The multiport transformer consists of three legs, each containing three independent phases belonging to a different inverter. Thus, each inverter has one phase in one of the legs of the transformer (see Fig. 3). This configuration enables magnetic coupling between the inductances.

It is crucial to consider both the self-inductances and the mutual inductances to ensure an accurate representation of the system. In Fig. 4 the representation of the self and mutual inductance of phase 1 of inverter A can be observed.
The expression for the voltages and currents of the windings in Eq. (1) is:

$$\begin{pmatrix} V_{1a} \\ V_{2a} \\ V_{3a} \\ \vdots \\ V_{3c} \end{pmatrix} = \begin{pmatrix} L_{1a} & M_{1a2a} & M_{1a3a} & \dots & M_{1a3c} \\ M_{2a1a} & L_{2a} & M_{2a3a} & \dots & M_{2a3c} \\ M_{3a1a} & M_{3a2a} & L_{3a} & \dots & M_{3a3c} \\ \vdots & \vdots & \vdots & \ddots & \vdots \\ M_{3c1a} & M_{3c2a} & M_{3c3a} & \dots & L_{3c} \end{pmatrix} \cdot \frac{d}{dt} \begin{pmatrix} I_{1a} \\ I_{2a} \\ I_{3a} \\ \vdots \\ I_{3c} \end{pmatrix} \quad (1)$$

Thanks to the symmetrical properties of the self-inductance and the mutual-inductance matrix, we acquire a 9x9 inductance matrix, where each parameter is easly measurable.

The calculation of power flow between inverters, based on phase shift control, necessitates a comprehensive consideration of various factors. Notably, the inclusion of self-inductances and mutual inductances for each phase within the inverter. In the context of phase shift control, understanding and quantifying the self-inductances of each phase are essential as they directly impact the energy exchange dynamics. By integrating these considerations into the calculation framework, a more accurate depiction of power flow dynamics between inverters under phase shift control can be achieved, enabling effective power flow management strategies.

In the referenced study [6], it was demonstrated that the inductance matrix provides a

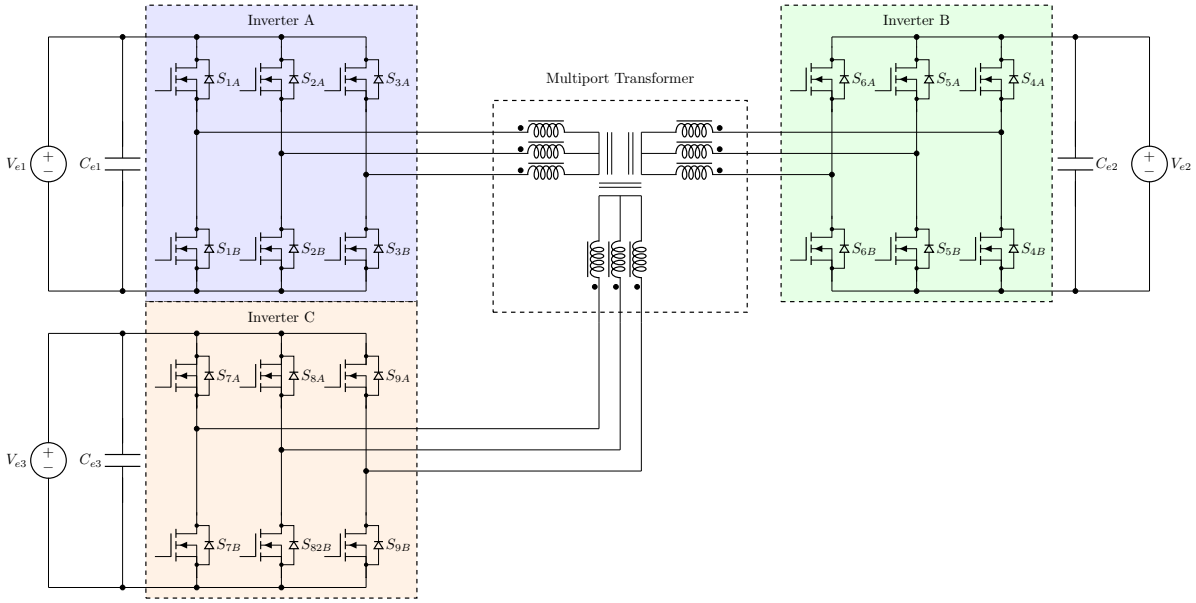

Fig. 2: Electrical circuit of the three-port three-phase multi-active bridge.

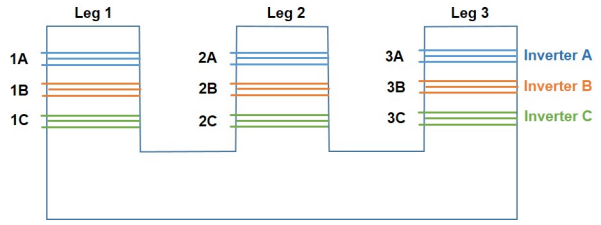

Fig. 3: Representation of the windings of the three-port transformer.

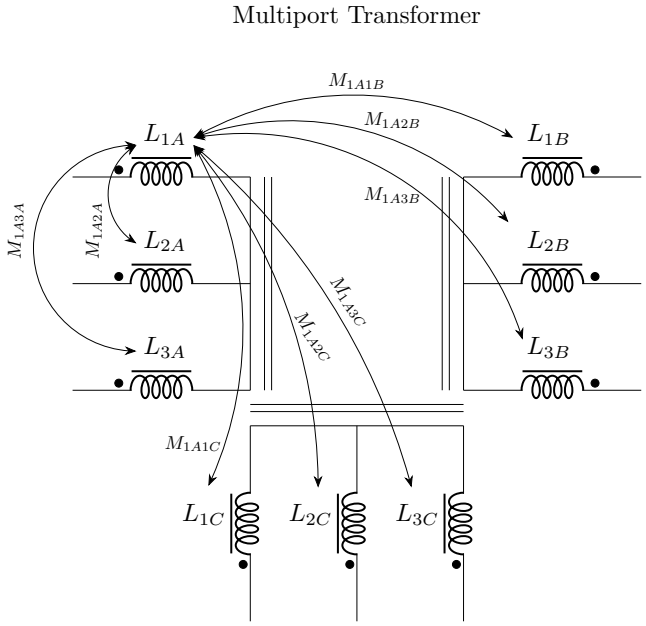

Fig. 4: Representation of the self and mutual inductance of phase 1 of inverter A.

method to establish a relationship between the magnetizing inductance and the leakage inductance inherent within the system. In references [7, 8], an N-branch transformer can be represented by an equivalent T-model, as illustrated in Fig. 5. The equivalent T-model [9,10] comprises a magnetic inductance, three leakage inductances, and an ideal transformer. The impedances and voltage sources of the inverters B and C are referred to the primary, which is in this case the inverter A. L_f represents the Leakage inductance and L_μ the Magnetizing inductance. The equivalent source

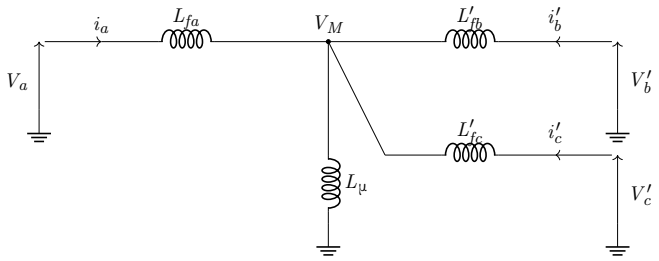

Fig. 5: T-model of the three-port transformer.

voltages at the B and C secondaries, as well as the related leakage inductances, are given by Eq. (2-7) [6].

$$K_{ab} = \frac{V_b}{V_a} = \frac{i_a}{i_b} = \frac{M_{C_{bc}}}{M_{C_{ac}}} \tag{2}$$

$$K_{ac} = \frac{V_c}{V_a} = \frac{i_a}{i_c} = \frac{M_{C_{bc}}}{M_{C_{ab}}} \tag{3}$$

$$L_\mu = \frac{M_{C_{ac}}.M_{C_{ab}}}{M_{C_{bc}}} \tag{4}$$

$$L_{fa} = L_{C_a} - \frac{M_{C_{ac}}.M_{C_{ab}}}{M_{C_{bc}}} \tag{5}$$

$$L'_{fb} = \frac{L_{C_b} - \frac{M_{C_{ab}}.M_{C_{bc}}}{M_{C_{ac}}}}{K^2_{ab}} \tag{6}$$

$$L'_{fc} = \frac{L_{C_c} - \frac{M_{C_{ac}}.M_{C_{bc}}}{M_{C_{ab}}}}{K^2_{ac}} \tag{7}$$

L_C "Cyclic self-inductance" represents the interaction between the self-inductance and the mutual inductances within the same inverter.
M_C represents the cyclic mutual inductance, which considers the effect between the mutual inductances within the same leg and those of the same inverter.
If we consider the equivalent T-model, taking phase 1 of each inverter as a reference, it is possible to quickly calculate the power supplied by the three energy sources (see Eq. (8)(9)(10)). V_M represents the midpoint potential, while V_a denotes the input voltage of inverter A and serves as a reference. Additionally, V_b and V_c represent the input voltages of inverters B and C, respectively, phased by angles φ_{ab} and φ_{ac} relative to V_a. Specifically, $V_a = [V_M; 0°]$, $V_b = [V_M; \varphi_{ab}]$, and $V_c = [V_M; \varphi_{ac}]$.

$$P_a = -\frac{3V_m^2.(\frac{sin(\varphi_{ab})}{L'_{fb}} + \frac{sin(\varphi_{ac})}{L'_{fc}})}{2L_{fa}.w.\alpha} \tag{8}$$

$$P_b = -\frac{3V_m^2.(\frac{sin(\varphi_{ab})}{L'_{fb}} + \frac{sin(\varphi_{ac})}{L'_{fc}} - sin(\varphi_{ab}).\alpha)}{2L'_{fb}.w.\alpha} \tag{9}$$

$$P_c = -\frac{3V_m^2.(\frac{sin(\varphi_{ab})}{L'_{fb}} + \frac{sin(\varphi_{ac})}{L'_{fc}} - sin(\varphi_{ac}).\alpha)}{2L'_{fc}.w.\alpha} \tag{10}$$

With $\alpha = (\frac{1}{L_\mu} + \frac{1}{L_{fa}} + \frac{1}{L'_{fb}} + \frac{1}{L'_{fc}})$.

2.3 Multiport Transformer Modeling

Effective modeling of the magnetic coupler proves essential during the converter's design phase, as outlined in reference [11]. This modeling process serves two critical purposes: firstly, it validates the converter's operational principles, and secondly, it facilitates optimization of the coupler's geometry for the intended application. Employing an analytical modeling approach based on a geometry-dependent reluctance model is key to achieving accurate representation of the magnetic coupler's behavior. By leveraging such modeling techniques, insights into the dynamic interactions within the magnetic coupler can be gained. These insights enable fine-tuning of design parameters, ensuring optimal performance and efficiency. Furthermore, this modeling approach supports informed decision-making throughout the design process. As depicted in Fig. 6, the transformer comprises upper and lower plates and cylindrical-shaped legs. This symmetrical configuration ensures an even distribution of port powers [12], resulting in equally sized inductances.

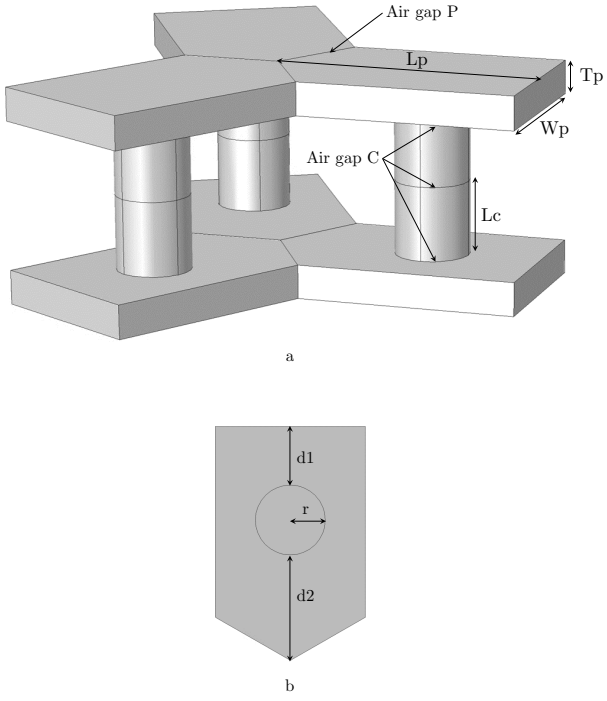

Fig. 6: 3D geometry of the three-port transformer.

The dimensions of the magnetic coupler are influenced by various parameters, including the length L_p and width W_p of both upper and lower plates, as well as the thickness T_p and air gap P between them. Additionally, factors such as the air

gaps C at the legs of the transformer, the length L_C and radius r of the transformer legs, and the distances $d1$ and $d2$ that define the position of the leg relative to the plate, play significant roles in determining its overall dimensions.

Taking into account a linear model for the magnetic behavior of the 3C90 material, characterized by a relative permeability (μr) of 2300, we can establish a straightforward reluctance model that relies on these parameters (see Fig. 7).

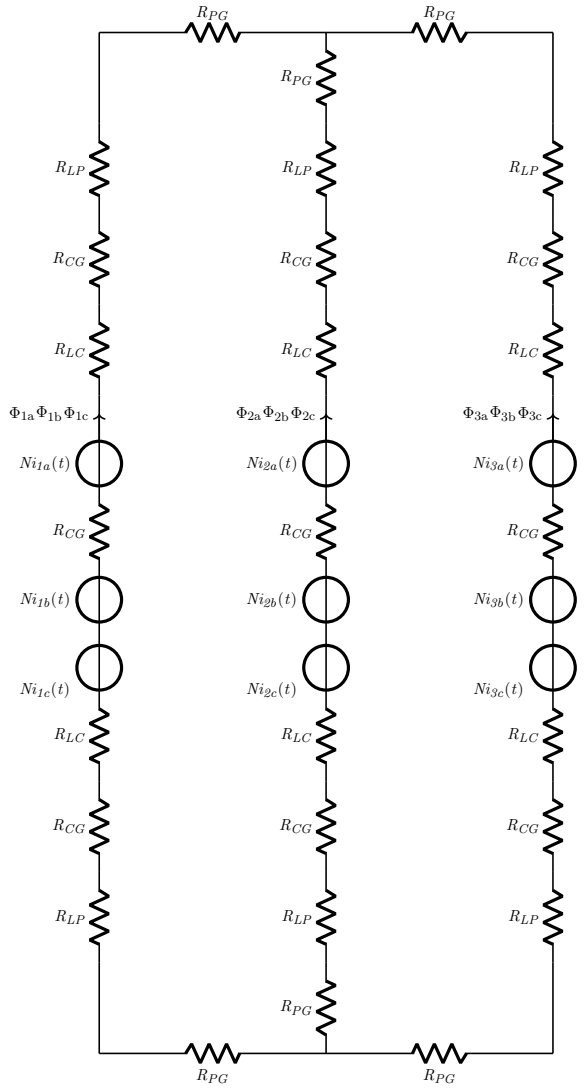

Fig. 7: Reluctance model circuit of the three-port transformer.

The reluctances R_{PG} (plates air gap), R_{LP} (plate), R_{CG} (leg air gap), and R_{LC} (leg) are defined by the following Eq. (11-14) :

$$R_{PG} = \frac{P}{\mu_0.S_{Pgap}} \tag{11}$$

$$R_{LP} = \frac{L_P - (d1 + r)}{\mu_0.\mu_r.S_P} \tag{12}$$

$$R_{CG} = \frac{C}{\mu_0.\pi r^2} \tag{13}$$

$$R_{LC} = \frac{L_C}{\mu_0.\mu_r.\pi r^2} \tag{14}$$

S_{Pgap} and S_P represent the cross-sectional area of the plate and the leg, respectively. The reluctance circuit, similar to an electrical circuit, enables the determination of equivalent reluctances seen from each source $N_i(t)$. This facilitates the determination of self-inductances L_i and mutual inductances M_{ij}, and the establishment of the theoretical inductance matrix based on the geometric parameters of the transformer. We obtain the following 9x9 inductance matrix (in μH) :

$$\begin{pmatrix}
3.10 & -1.55 & -1.55 & 3.10 & -1.55 & -1.55 & 3.10 & -1.55 & -1.55 \\
-1.55 & 3.10 & -1.55 & -1.55 & 3.10 & -1.55 & -1.55 & 3.10 & -1.55 \\
-1.55 & -1.55 & 3.10 & -1.55 & -1.55 & 3.10 & -1.55 & -1.55 & 3.10 \\
3.10 & -1.55 & -1.55 & 3.10 & -1.55 & -1.55 & 3.10 & -1.55 & -1.55 \\
-1.55 & 3.10 & -1.55 & -1.55 & 3.10 & -1.55 & -1.55 & 3.10 & -1.55 \\
-1.55 & -1.55 & 3.10 & -1.55 & -1.55 & 3.10 & -1.55 & -1.55 & 3.10 \\
3.10 & -1.55 & -1.55 & 3.10 & -1.55 & -1.55 & 3.10 & -1.55 & -1.55 \\
-1.55 & 3.10 & -1.55 & -1.55 & 3.10 & -1.55 & -1.55 & 3.10 & -1.55 \\
-1.55 & -1.55 & 3.10 & -1.55 & -1.55 & 3.10 & -1.55 & -1.55 & 3.10
\end{pmatrix}$$

In the analysis of a magnetic circuit within the framework of the linear approximation of Hopkinson [13], it involves perfect magnetic circuits. These circuits are linear (with constant relative permeability μr) and free from magnetic leaks (where all the flux created by the windings appears in the magnetic circuit). Therefore, it is not possible to determine leakage inductances from this theoretical inductance matrix.

To complete the modeling of the transformer, finite element analysis allows for electromagnetic simulation of the transformer in 3D. Thanks to the software COMSOL Multiphysics we can obtain the magnetic induction in the transformer under nominal operating conditions (see Fig. 8).

The voltage applied across the terminals of the transformer windings is 33V at a frequency of 50kHz. The maximum inductance in the transformer is approximately 200mT, which falls within the linear zone of the $B(H)$ curve of the 3C90 material. This confirms that it is well below the saturation point, and that the transformer operates within the desired parameters and ensures its effective functionality.

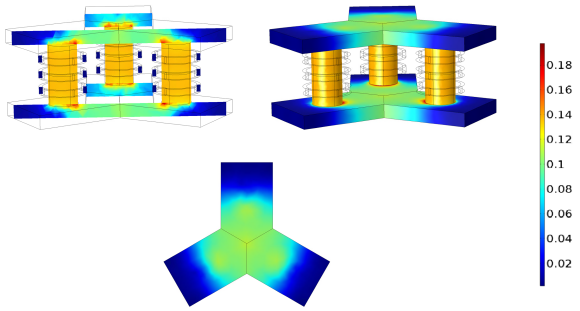

Fig. 8: 3D simulation of the magnetic induction (mT) of the three-port transformer.

This electromagnetic simulation also facilitates the extraction of the inductance matrix by employing the method of measuring the open-circuit voltage at each winding when a driving voltage is applied to the other winding. Equations (15) and (16) allow for the calculation of the self and mutual inductances.

$$L_i = \frac{1}{w} Im(\frac{V_{coil}i}{I_{coil}i}) \tag{15}$$

$$M_{ij} = \frac{1}{w} Im(\frac{V_{coil}j}{I_{coil}i}) \tag{16}$$

We obtain the following 9x9 inductance matrix (in μH) :

$$\begin{pmatrix}
3.2432 & -1.1384 & -1.1385 & 3.0203 & -1.1360 & -1.1360 & 2.9065 & -1.1361 & -1.1361 \\
-1.1384 & 3.2433 & -1.1387 & -1.1360 & 3.0206 & -1.1363 & -1.1361 & 2.9067 & -1.1364 \\
-1.1385 & -1.1387 & 3.2432 & -1.1360 & -1.1363 & 3.0204 & -1.1361 & -1.1364 & 2.9066 \\
3.0203 & -1.1360 & -1.1360 & 3.1753 & -1.1348 & -1.1348 & 3.0177 & -1.1360 & -1.1360 \\
-1.1360 & 3.0206 & -1.1363 & -1.1348 & 3.1754 & -1.1351 & -1.1360 & 3.0180 & -1.1363 \\
-1.1360 & -1.1363 & 3.0204 & -1.1348 & -1.1351 & 3.1754 & -1.1360 & -1.1362 & 3.0178 \\
2.9065 & -1.1361 & -1.1361 & 3.0177 & -1.1360 & -1.1360 & 3.2432 & -1.1384 & -1.1384 \\
-1.1361 & 2.9067 & -1.1364 & -1.1360 & 3.0180 & -1.1362 & -1.1384 & 3.2435 & -1.1387 \\
-1.1361 & -1.1364 & 2.9066 & -1.1360 & -1.1363 & 3.0178 & -1.1384 & -1.1387 & 3.2432
\end{pmatrix}$$

With this matrix, we can either determine the leakage inductances and calculate the power flow $P = f[\phi_{AB}, \phi_{Ac}]$ from Eq. (8-10) or simulate the converter on Ltspice by coupling the inductances using the coupling coefficient k_{ij} Eq. (17).

$$k_{ij} = \frac{M_{ij}}{\sqrt{L_i L_j}} \tag{17}$$

2.4 Simulation of the Converter

With simulation we can accurately replicate and analyze the behavior of the converter. Through comprehensive simulation and modeling techniques, we can assess various performance metrics, including efficiency, voltage regulation, and power transfer characteristics.

We can compare the results obtained from different methods. Tables 1 and 2 present the power flow between the inverters for different phase-shifts, with Table 1 corresponding to a phase-shift of $\phi_{AB} = \phi_{AC} = -10°$, and Table 2 corresponding to a phase-shift of $\phi_{AB} = \phi_{AC} = -20°$. Comparing these results provides valuable insights on the power exchange dynamics between the inverters.

	$P_A(W)$	$P_B(W)$	$P_C(W)$
Theoretical	-1979	1320	495
T-model	-1979	1320	495
LTspice	-2048	1424	458
COMSOL	-1976	1457	467

Tab. 1: Power flow for $\phi_{AB} = \phi_{AC} = -10°$

	$P_A(W)$	$P_B(W)$	$P_C(W)$
Theoretical	-4032	2395	1021
T-model	-4032	2395	1021
LTspice	-4165	2587	955
COMSOL	-3907	2739	973

Tab. 2: Power flow for $\phi_{AB} = \phi_{AC} = -20°$

The results obtained from these different methods reveal that when negative phase-shifts are applied to inverters B and C, inverter A supplies power to inverters B and C. The negative sign of the power value indicates that it supplies power, whereas a positive value indicates that it receives power. This analysis sheds light on the directional flow of power within the system and underscores the significance of phase-shift control in regulating energy exchange between the inverters.

In the case of the Theoretical and the T-model we obtain the same results. Despite the similarity in magnitudes, differences emerge between the LTspice, COMSOL, Theoretical, and T-model results. This discrepancy stems from the theoretical and T-models not accounting for magnetic flux leakage, as they operate within the linear approximation of Hopkinson, assuming perfect magnetic circuits. Consequently, these models may not fully capture the complexities of real-world behavior, resulting in variations in the simulated results compared to those obtained from software simulations like LTspice and COMSOL.

Until this stage, all simulations have utilized a sinu-

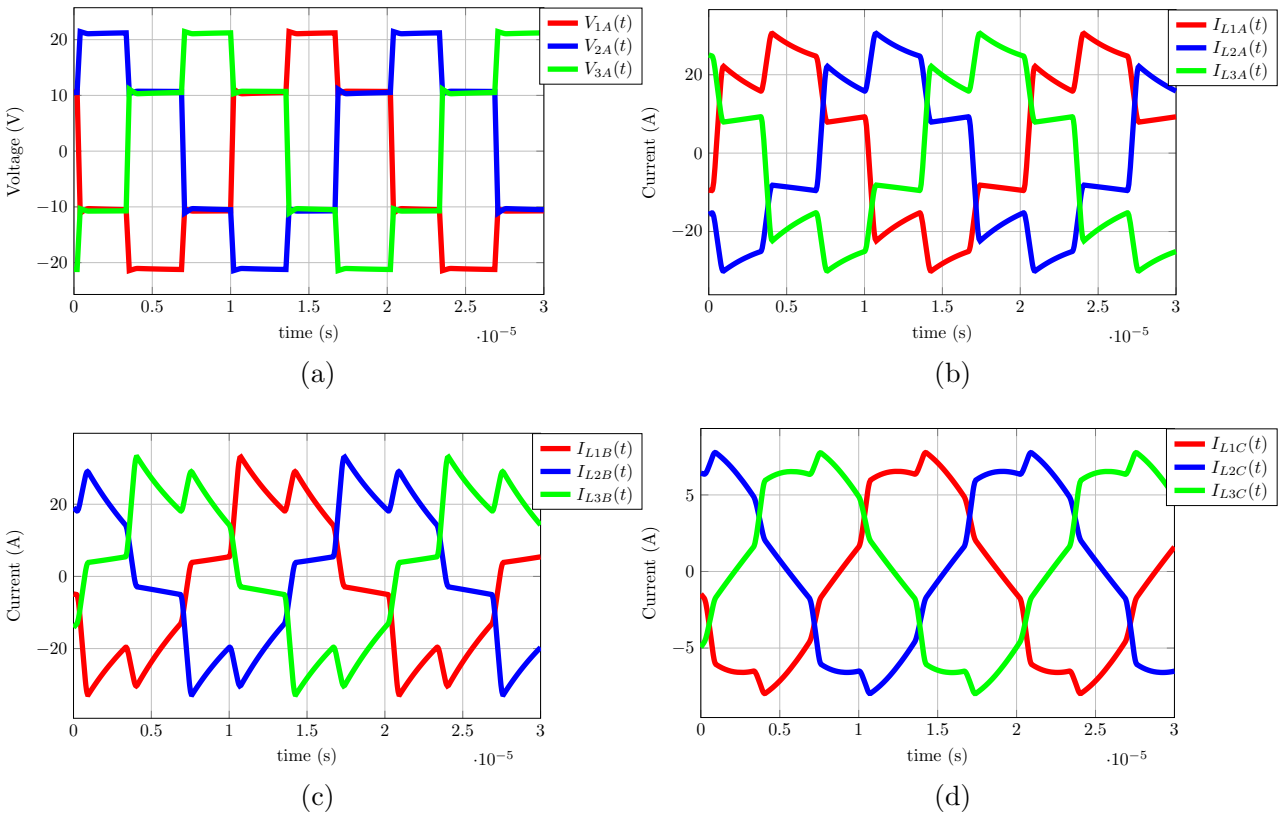

Fig. 9: Simulation results. (a) voltages of the three phases of inverter A. (b) currents in the windings of inverter A. (c) currents in the windings of inverter B. (d) currents in the windings of inverter C.

soidal waveform voltage. However, the converter will employ a six-step control. In Fig. 9, the waveforms and amplitudes of the voltage across the transformer windings, as well as the currents flowing through each transformer winding, are illustrated. The simulations conducted on LTspice using six-step control enable us to anticipate the behavior of the converter prior to experimental testing. This provides us with the opportunity to analyze the voltage and current waveforms for different phase-shifts.

3 Experimental Testing of the Converter

Figure 10 the transformer has been fabricated and assembled, featuring plates and legs with cylindrical shapes, constructed using 3C90 material. Within the transformer, the PCBs of the three inverters integrate the windings, each coil comprising $N = 2$ turns. These PCBs are arranged in a stacked configuration. The control board regulates the switches of the inverters, facilitated by rotary encoders, allowing for precise adjustment of the switching frequency and phase shifts ϕ_{AB} and ϕ_{AC}. Experimental testing is conducted under open-loop control conditions.

Following the completion of the converter, the actual inductance matrix was measured using an impedance analyzer. Subsequently, the measured matrix was compared with both the theoretical matrix extracted from the reluctance model and the finite element analysis matrix extracted from the electromagnetic simulation using COMSOL software. This comprehensive

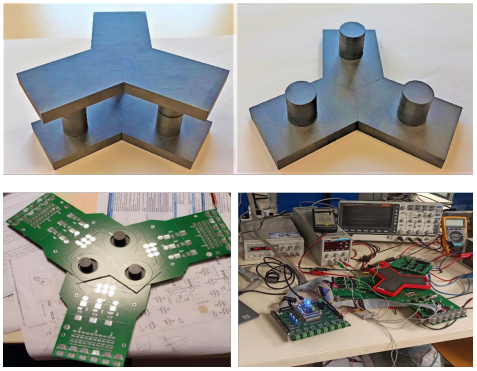

Fig. 10: Experimental setup of the three-port three-phase Multi-Active Bridge converter.

comparison enabled a thorough validation of

the theoretical predictions and simulation results against empirical measurements. Such validation is essential for ensuring the accuracy and reliability of the theoretical and simulation-based approaches in predicting the transformer's behavior and performance under various operating conditions. We obtain the following 9x9 inductance matrix (in μH) :

$$\begin{pmatrix} 3.32 & -0.91 & -0.96 & 3.00 & -1.08 & -1.10 & 2.86 & -1.10 & -1.12 \\ -0.93 & 3.55 & -1.22 & -1.05 & 3.24 & -1.35 & -1.08 & 3.08 & -1.37 \\ -0.99 & -1.23 & 3.76 & -1.09 & -1.36 & 3.41 & -1.10 & -1.39 & 3.28 \\ 3.02 & -1.06 & -1.10 & 3.19 & -1.10 & -1.12 & 3.03 & -1.08 & -1.13 \\ -1.08 & 3.22 & -1.36 & -1.10 & 3.35 & -1.40 & -1.09 & 3.24 & -1.38 \\ -1.11 & -1.36 & 3.40 & -1.10 & -1.35 & 3.52 & -1.12 & -1.35 & 3.42 \\ 2.91 & -1.08 & -1.13 & 3.00 & -1.12 & -1.15 & 3.22 & -1.11 & -1.14 \\ -1.10 & 3.12 & -1.39 & -1.12 & 3.20 & -1.39 & -1.07 & 3.40 & -1.38 \\ -1.13 & -1.39 & 3.30 & -1.15 & -1.41 & 3.39 & -1.10 & -1.35 & 3.68 \end{pmatrix}$$

The initial tests of this converter were conducted with an input voltage of $V_{in} = 20V$ for each inverter, employing a switching frequency of $F_S = 50kHz$, and allowing for phase shifts ϕ_{AB} and ϕ_{AC} to vary within the range of $-10° \leq \phi \leq 13°$. These tests aimed to explore the converter's behavior under different phase-shift configurations and provide insights into its operational characteristics across a broad spectrum of operating conditions.

We can graphically represent the relationship between exchanged powers and phase shifts in Fig. 11. This graphical representation allows for a clear visualization of how changes in phase shift affect the power exchange dynamics between the inverters. By analyzing this evolution, we can gain valuable insights into the optimal phase-shift settings for maximizing power transfer efficiency and achieving desired operational performance.

The power mapping of the converter illustrates the validity of the Multi-Active Bridge's operating principle and showcases its capability to regulate energy exchange between different sources through the adjustment of phase shifts between the inverters. This validation underscores the effectiveness of the converter's design in facilitating dynamic control and efficient management of power flow, highlighting its potential for various applications requiring precise energy distribution and control.
In Fig. 12, the waveforms and amplitudes of the voltage across the transformer windings, as well as the currents, depict the maximum currents for each inverter, with phase shifts ranging from -10° to 13°. Each inverter is configured with a specific

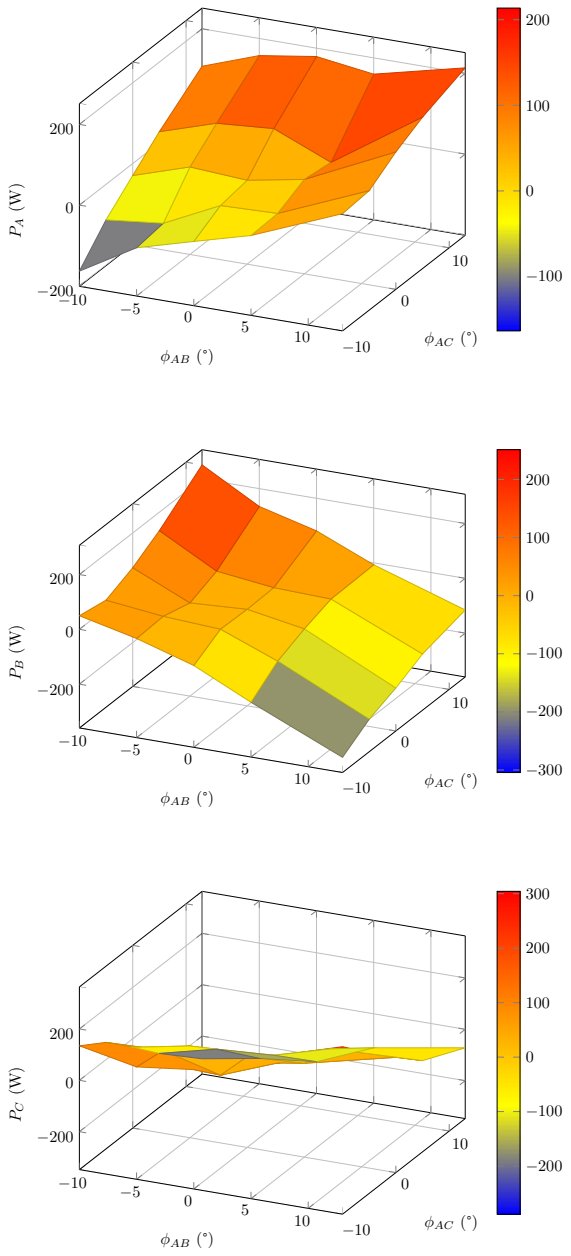

Fig. 11: Experimental power mapping of the three-port three-phase Multi-Active Bridge converter.

phase shift combination to achieve its peak current. For inverter A, the current reaches its maximum when both ϕ_{AB} and ϕ_{AC} are set to -10°. In the case of inverter B, the current peaks at $\phi_{AB} = 13$ and $\phi_{AC} = 10$. Similarly, for inverter C, the current reaches its peak at $\phi_{AB} = -10$ and $\phi_{AC} = 13$. This detailed analysis provides valuable insights into the optimal phase shift configurations for maximizing current flow in each inverter, facilitating informed decision-making during system optimization and

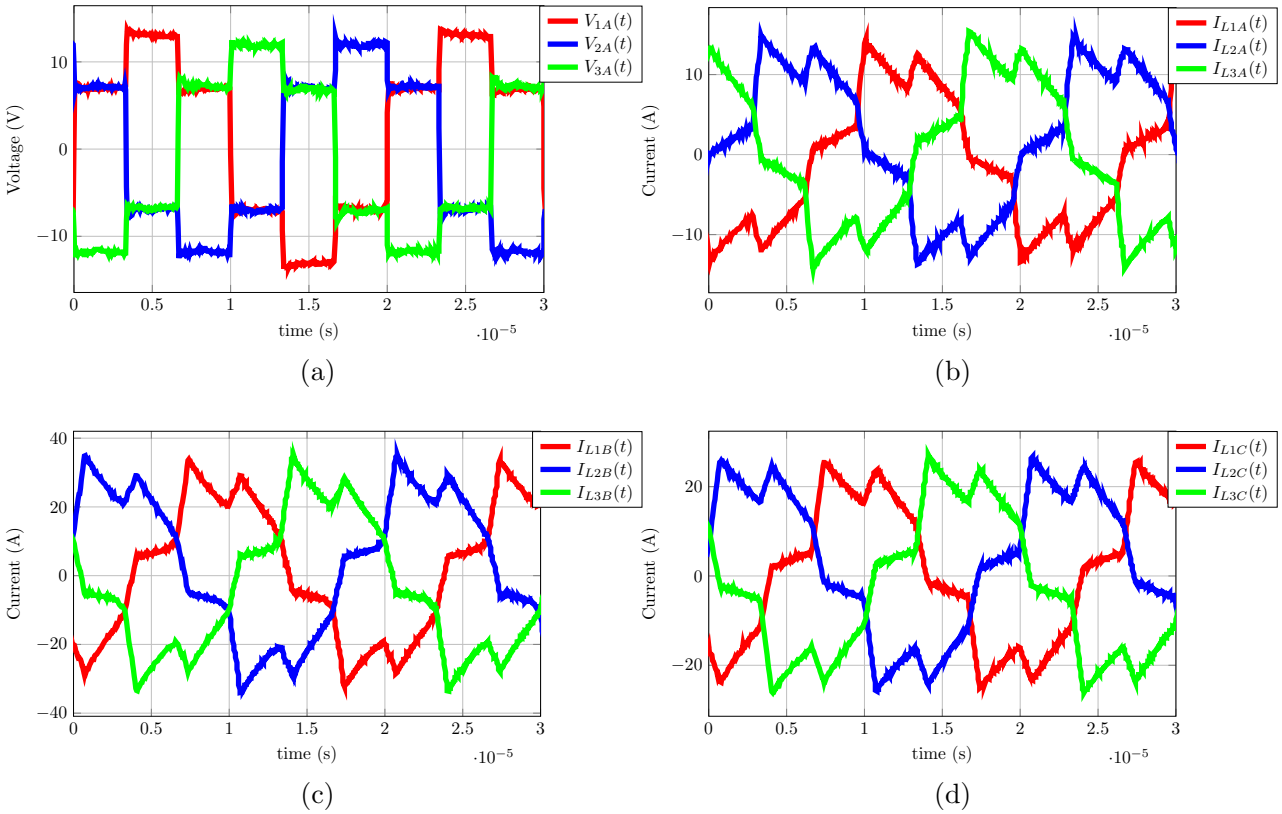

Fig. 12: Experimental results. (a) voltages of the three phases of inverter A. (b) currents in the windings of inverter A. (c) currents in the windings of inverter B. (d) currents in the windings of inverter C.

control design. The Multi-Active-Bridge relies heavily on the low values of leakage and magnetizing inductances of the transformer, typically in the microhenry range.

4 Conclusion

This study presents the design and implementation of a three-port, three-phase Multi-Active Bridge (MAB) converter, designed to enhance the integration of renewable energy sources into domestic electrical grids. Through theoretical insights, simulations, and practical experiments, we demonstrated the converter's efficient management of bidirectional energy flow, highlighting its potential to address renewable energy's intermittency. The converter's phase-shift control and magnetic coupling transformer prove effective in optimizing energy transfer, promising significant advancements in sustainable domestic energy management. Our work lays a foundation for future developments in smart grid technologies, emphasizing the importance of renewable energy integration for a sustainable energy future.

5 Acknowledgements

I would like to express my gratitude to Labex Solstice for providing the funding that supported the research presented in this article.

References

[1] S. Adams et A. O. Acheampong, « Reducing carbon emissions: The role of renewable energy and democracy », Journal of Cleaner Production, vol. 240, p. 118245, déc. 2019, doi: 10.1016/j.jclepro.2019.118245.

[2] O. Wildgruber, « Hydrogen as Energy Source: An Introduction », Energy Environment, vol. 17, n 2, p. 275-279, mars 2006, doi: 10.1260/095830506777070114.

[3] A. Merrouche et al., « Convertisseur multi-sources solaire pour pile à hydrogène », in Journées Nationales du Photovoltaïque 2022, Dourdan, France, nov. 2022. Consulté le: 7 avril 2024. [En ligne]. Disponible sur: https://hal.science/hal-03887957

[4] H. Tao, A. Kotsopoulos, J. L. Duarte, and M. a. M. Hendrix, "Family of multiport bidi-

rectional DC–DC converters," IEE Proceedings - Electric Power Applications, vol. 153, no. 3, pp. 451–458, May 2006, doi: 10.1049/ip-epa:20050362.

[5] H. Qin, H. Zhang, M. Liu, and C. Ma, "Comparison of Different Multi-winding Transformer Models in Multi-port AC-coupled Converter Application," in IECON 2021 – 47th Annual Conference of the IEEE Industrial Electronics Society, Toronto, ON, Canada: IEEE, Oct. 2021, pp. 1–6. doi: 10.1109/IECON48115.2021.9589283.

[6] G. Pellecuer, T. Martire, M. Petit and B. Loyer, "On-Board Power Management in a Marine Autonomous Surface Vehicle (ASV): Multi-Port Transformer Design," PCIM Europe 2022; International Exhibition and Conference for Power Electronics, Intelligent Motion, Renewable Energy and Energy Management, Nuremberg, Germany, 2022, pp. 1-9, doi: 10.30420/565822275.

[7] H. Tao, A. Kotsopoulos, J. L. Duarte and M. A. M. Hendrix, "A Soft-Switched Three-Port Bidirectional Converter for Fuel Cell and Supercapacitor Applications," 2005 IEEE 36th Power Electronics Specialists Conference, 2005, pp. 2487-2493,doi: 10.1109/PESC.2005.15819

[8] C. Sun, N. H. Kutkut, D. W. Novotny, et D. M. Divan, " General equivalent circuit of a multiwinding co-axial winding transformer ", in IAS '95. Conference Record of the 1995 IEEE Industry Applications Conference Thirtieth IAS Annual Meeting, 1995, vol. 3, p. 2507-2514 vol.3. doi: 10.1109/IAS.1995.530622.

[9] J. G. Hayes, N. O'Donovan, and M. G. Egan, "The extended T model of the multiwinding transformer," in 2004 IEEE 35th Annual Power Electronics Specialists Conference (IEEE Cat. No.04CH37551), Aachen, Germany: IEEE, 2004, pp. 1812–1817. doi: 10.1109/PESC.2004.1355391.

[10] H. Shi-Ping, "Problems in Analysis and Design of Switching Regulators," California Institute of Technology, 1979.

[11] J. Yang, G. Buticchi, C. Gu, S. Gunter, H. Zhang, and P. Wheeler, "A Generalized Input Impedance Model of Multiple Active Bridge Converter," IEEE Trans. Transp. Electrific., vol. 6, no. 4, pp. 1695–1706, Dec. 2020, doi: 10.1109/TTE.2020.2986604.

[12] Neubert, M. (2020). Modeling, synthesis and operation of multiport-active bridge converters (Doctoral dissertation, Dissertation, Rheinisch-Westfälische Technische Hochschule Aachen, 2020).

[13] D. W. Jordan, "The Magnetic Circuit Model, 1850–1890: The Resisted Flow Image in Magnetostatics," The British Journal for the History of Science, vol. 23, no. 2, pp. 131–173, Jun. 1990, doi: 10.1017/S0007087400044733.